Available online at www.sciencedirect.com
ScienceDirect
Journal of Petroleum Science and Engineering 56 (2007) 108 – 126
JOURNAL OF PETROLEUM SCIENCE & ENGINEERING
www.elsevier.com/locate/petrol

Methane hydrate formation and dissociation in a partially saturated core-scale sand sample

Timothy J. Kneafsey [a,*], Liviu Tomutsa [a], George J. Moridis [a], Yongkoo Seol [a],
Barry M. Freifeld [a], Charles E. Taylor [b], Arvind Gupta [c]

[a] Lawrence Berkeley National Laboratory, 1 Cyclotron Rd, Berkeley, CA 94720, United States
[b] National Energy Technology Laboratory, 626 Cochrans Mill Rd, Pittsburgh, PA 15236-0940, United States
[c] Colorado School of Mines, PO Box 4028, Golden, CO 80401-1887, United States

Accepted 3 February 2006

Abstract

We performed a series of experiments to provide data for validating numerical models of gas hydrate behavior in porous media. Methane hydrate was formed and dissociated under various conditions in a large X-ray transparent pressure vessel, while pressure and temperature were monitored. In addition, X-ray computed tomography (CT) was used to determine local density changes during the experiment. The goals of the experiments were to observe changes occurring due to hydrate formation and dissociation, and to collect data to evaluate the importance of hydrate dissociation kinetics in porous media. In the series of experiments, we performed thermal perturbations on the sand/water/gas system, formed methane hydrate, performed thermal perturbations on the sand/hydrate/water/gas system resulting in hydrate formation and dissociation, formed hydrate in the resulting partially dissociated system, and dissociated the hydrate by depressurization coupled with thermal stimulation. Our CT work shows significant water migration in addition to possible shifting of mineral grains in response to hydrate formation and dissociation. The extensive data including pressure, temperatures at multiple locations, and density from CT data is described.
Published by Elsevier B.V.

Keywords: Hydrate formation; Dissociation; Porous medium; Thermal stimulation; Depressurization; X-ray computed tomography

1. Introduction

Gas hydrates in the earth's subsurface within permafrost and sub-sea environments are thought to hold a vast amount of potentially producible natural gas (Sloan, 1998). Each cubic meter of gas hydrate can hold approximately 160 m^3 of natural gas at standard temperature and pressure (STP) (National Resource Council, 2004). Because gas hydrates are unstable at STP and recovered samples have all been transported through conditions different from where they originated, measurements on the recovered samples have not provided adequate information for simulation of natural gas production from hydrate-bearing reservoirs.

Information needed to reliably predict the feasibility of producing natural gas from hydrates includes:

- Abundance of the hydrates in the selected reservoir
- Lithology and geologic structure of the reservoir

---

[*] Corresponding author. Fax: +1 510 486 5686.
E-mail address: TJKneafsey@lbl.gov (T.J. Kneafsey).

0920-4105/$ - see front matter. Published by Elsevier B.V.
doi:10.1016/j.petrol.2006.02.002

- Presence or absence of a free gas zone
- Arrangement of hydrate within the porous medium
- Permeability, relative permeability–saturation relationships, capillary pressure–saturation relationships, and thermal conductivity of the hydrate-bearing and hydrate-free medium
- Energy required to dissociate the hydrate (how close the hydrate is to equilibrium)
- Kinetics of dissociation.

Several of these information needs are reservoir specific, but others – such as dissociation kinetics, thermal conductivity, and relative permeability – have components of general applicability that can be evaluated in the laboratory.

Both laboratory-made and natural hydrate samples can be used in laboratory studies. Natural hydrate samples are not abundantly available and can be somewhat-to-severely compromised by collection, recovery, transport, and handling. Several methods are available for making hydrates in a porous medium, including the method used by Stern et al. (1996) which converts granulated ice into hydrate by controlled melting at excess methane pressure, and the method of Handa and Stupin (1992) that converts capillary-held water into hydrate at excess methane pressure. Scanning electron microscopy has been used to compare natural samples to samples made using Stern's method, and the samples appear nearly identical (Stern et al., 2004). The conditions of these observations, however, are <105 K and 10^{-3} Pa, whereas the natural environment for the samples is moderate pressure (~3 to 10 MPa) and above-freezing temperatures (several °C).

Samples made in quartz sand using Handa's method are thought to cement sand grains (Waite et al., 2004), whereas hydrates at the Mallik site in northern Canada are thought to be part of the solid frame of the sediment (Winters et al., 2004). The hydrate configuration (cementing or solid frame) may affect properties such as the thermal conductivity and relative permeability of the hydrate-bearing sediment. Because natural samples have likely been at least partially compromised, and laboratory-made samples are thought to have some characteristics unlike natural hydrate bearing sediments, results from measurements on either laboratory-made or natural samples must be regarded with caution.

The kinetics of hydrate dissociation have been measured in laboratory stirred tank semibatch reactors (Kim et al., 1987; Clarke and Bishnoi, 2001). The effect of kinetics has not been experimentally investigated in porous medium samples containing hydrate, particularly in light of heat- and mass-transfer interferences. Kinetic effects may affect natural gas production from a hydrate-bearing reservoir, consequently, these effects must be considered.

In this work, we performed a sequence of tests on a partially water-saturated sand sample contained in an X-ray-transparent aluminum pressure vessel. These tests were performed to (1) observe changes that occur in response to hydrate formation and dissociation, and (2) gather information to evaluate the kinetic nature of hydrate dissociation in a partially saturated porous medium. The test sequence included preliminary tests to monitor the vessel strain during hydrate formation and dissociation, tests to allow computation of sample thermal conductivity, hydrate formation, dissociation by thermal stimulation, another hydrate formation step, and dissociation by depressurization coupled with thermal stimulation. Numerical modeling of these tests to determine thermal conductivities and kinetic parameters will be presented elsewhere (e.g. Moridis et al., 2005).

2. Equipment and materials

2.1. Pressure vessel

The pressure vessel used in this experiment was a 7.62 cm inner diameter and 8.9 cm outer diameter aluminum tube with threaded stainless steel end caps (Fig. 1). The end caps set the inner axial length to 31.75 cm. One of the end caps was machined to provide four feed-throughs for thermocouples. The other end was machined to provide a connection to the gas source. Three of four Type-T thermocouples (18 in. long, 1/16 in. diameter, stainless steel shielded ungrounded, Omega Engineering, Stamford, CT) were placed in a vertical line, with one about 0.5 cm from the top, one about 0.5 cm from the bottom, and one near the center (see Fig. 1, Section A-A′). This arrangement was selected to monitor the effect of a water saturation gradient caused by gravity in the partially saturated sand. The fourth thermocouple was placed in the horizontal midplane, approximately 0.5 cm from the vessel wall. The exact locations of the thermocouples were determined from X-ray computed tomography (CT) images (e.g., Fig. 5). System pressure was measured on the line connected to the pressure vessel using a Rosemount 1151 pressure transducer. Because water was placed in the sand prior to the experiment and the line was used only to carry gas, we assumed that pressure communication with the sample was direct and that there were no blockages in the line between the transducer and the sample.

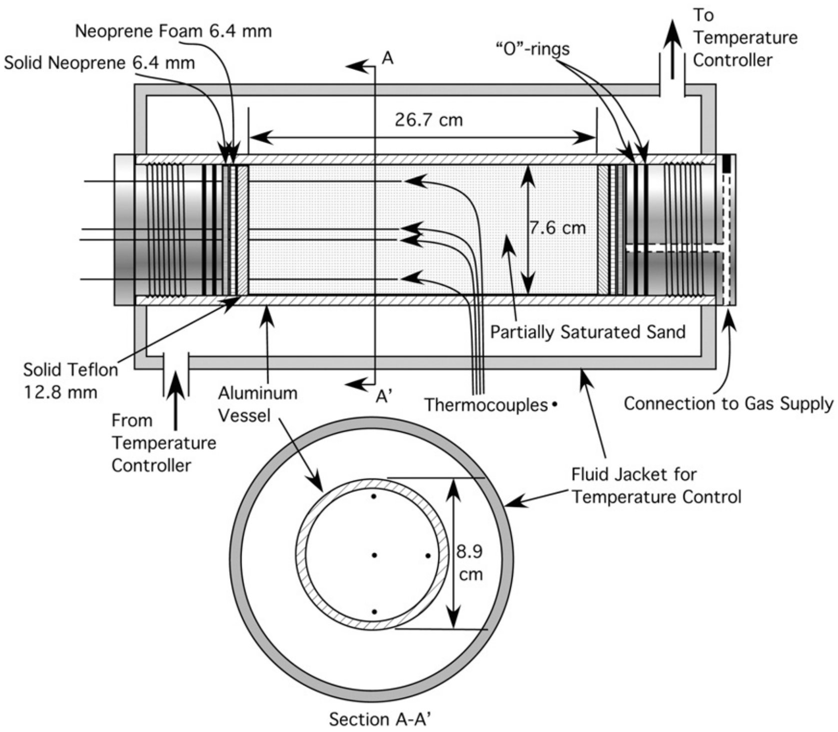

Fig. 1. Pressure vessel schematic.

2.2. Sand and preparation

The sand used in this experiment was Foundry 110, (U.S. Silica, Berkeley Springs WV, lot 111750071802). This silica sand consists of rounded to subangular grains primarily in the 100 to 200 μm grain size (Fig. 2). The sand was step-wise moistened with distilled, deionized water in a plastic bag, with considerable mixing between water additions until the desired moisture content was achieved and the water was perceived to be uniformly distributed. The moistened sand was packed into the pressure vessel from the gas introduction side in lifts of about 1.5 cm, using a 1.3 cm diameter steel rod (in the region with the thermocouples to access the space between them) or a 2.5 cm diameter aluminum rod (away from the thermocouples) with about 70 blows per lift. In this manner, 2219.5 g of the sand/water mixture was packed into the cell (244 g water) to a porosity of 38.7% and water saturation of 0.52. Steel tubes (6 mm o.d.) were placed over the thermocouples during sand packing to protect the thermocouples and help in placement. These tubes were lifted as each sand layer was added during the packing; however, in some locations, this resulted in poorer packing around the thermocouples. In spite of this poorer packing, the temperature indicated by the thermocouples would be substantially the same as the immediate environment of the thermocouple tip because of the test geometry and the amount of thermal contact between the sample and the thermocouples.

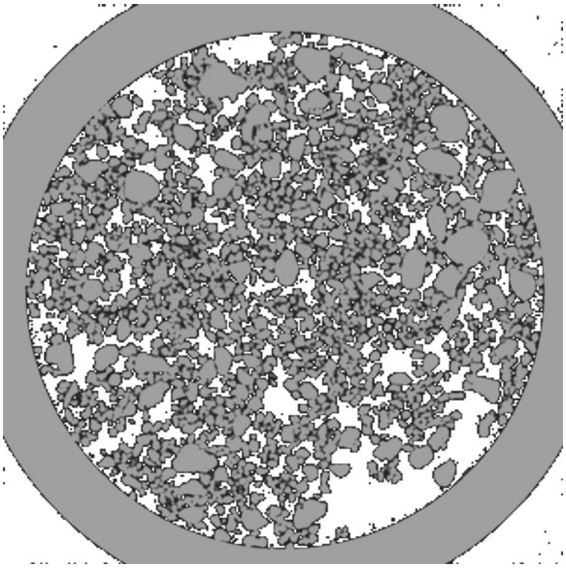

Fig. 2. X-ray computed microtomography image of poorly packed Foundry-110 sand in a small pressure vessel. The outer diameter of the gray circle (an aluminum pressure vessel) is 6 mm. The sand grains are gray, water is black, and gas is white.

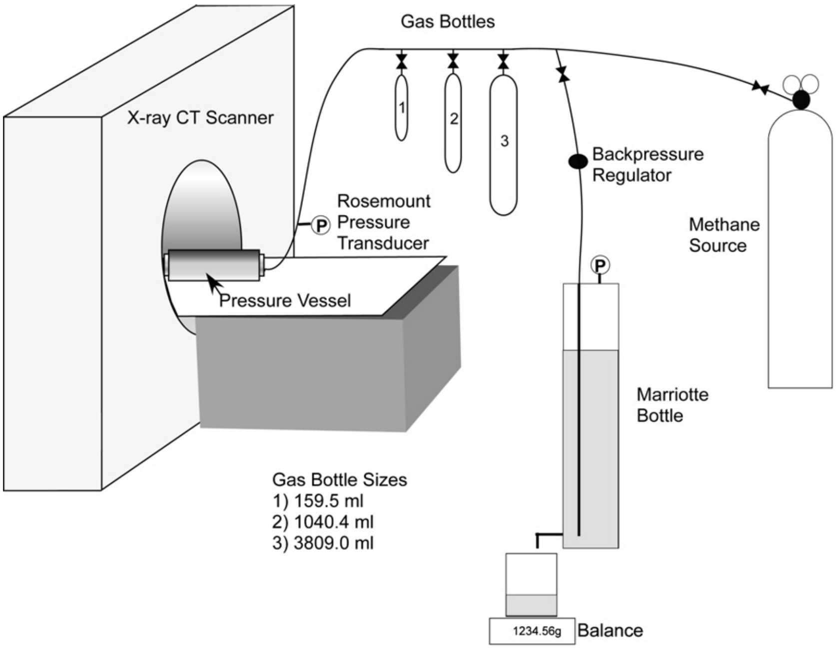

Fig. 3. Experiment setup.

2.3. CT scanning

The vessel was inserted into the fluid jacket, and the fluid jacket was attached to a temperature controller to allow the flow of temperature-controlled water/propylene glycol over the outside of the vessel. The pressure vessel/fluid jacket assembly was attached to the CT scanner table (Fig. 3), and insulated. The CT scanner

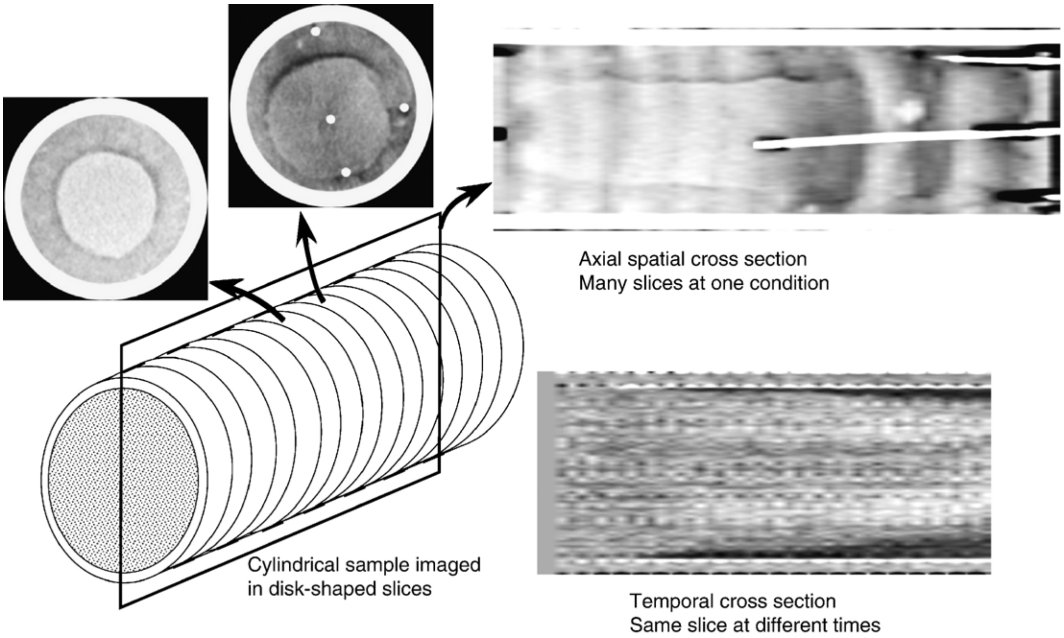

Fig. 4. X-ray CT imaging and image presentation. Disk-shaped cross sections were initially collected (top left). The data can be reconstructed to provide other views such as the axial spatial cross section (top right). By scanning a single location over time, a temporal cross section can be constructed showing changes at that location (lower right).

(Seimens Somatom HiQ, third-generation modified medical CT scanner) was used to obtain disk-shaped cross-sectional scans of the cylindrical vessel. We used a 0.5 cm scan thickness, resulting in voxels (constant volume regions of space for which densities are calculated) of about 0.25 × 0.25 × 5 mm, requiring 58 scans to adequately cover the vessel (including the Teflon spacers). Each voxel is about 600 times the size of a 100-μm-diameter sphere representing a typical sand grain. Each scan contains 512 × 512 voxels; those shown in this paper were cropped to contain only the 310 × 313 voxels pertaining to the pressure vessel and sample, not the fluid jacket. The CT data were calibrated to known standards (air, water plus propylene glycol, and water plus sand) for the density measurements presented here.

The CT scanner can be used to collect information on spatial density distribution if a series of locations are scanned, and also temporal changes if a set of locations are repeatedly scanned over the time when changes occur (Fig. 4). Additionally, the CT data can be assembled to display views other than the disk-shaped cross sections, such as axial cross sections or the temporal evolution of a cross section. In this paper, disk-shaped cross sections of density and density changes, and temporal vertical axial cross sections of density changes (such as the lower right image of Fig. 4), are presented.

Initial CT scans following the pre-test showed a heterogeneous structure within the sand/water sample (Fig. 5), in spite of our attempts to homogeneously pack the vessel. In these scans, higher density regions are

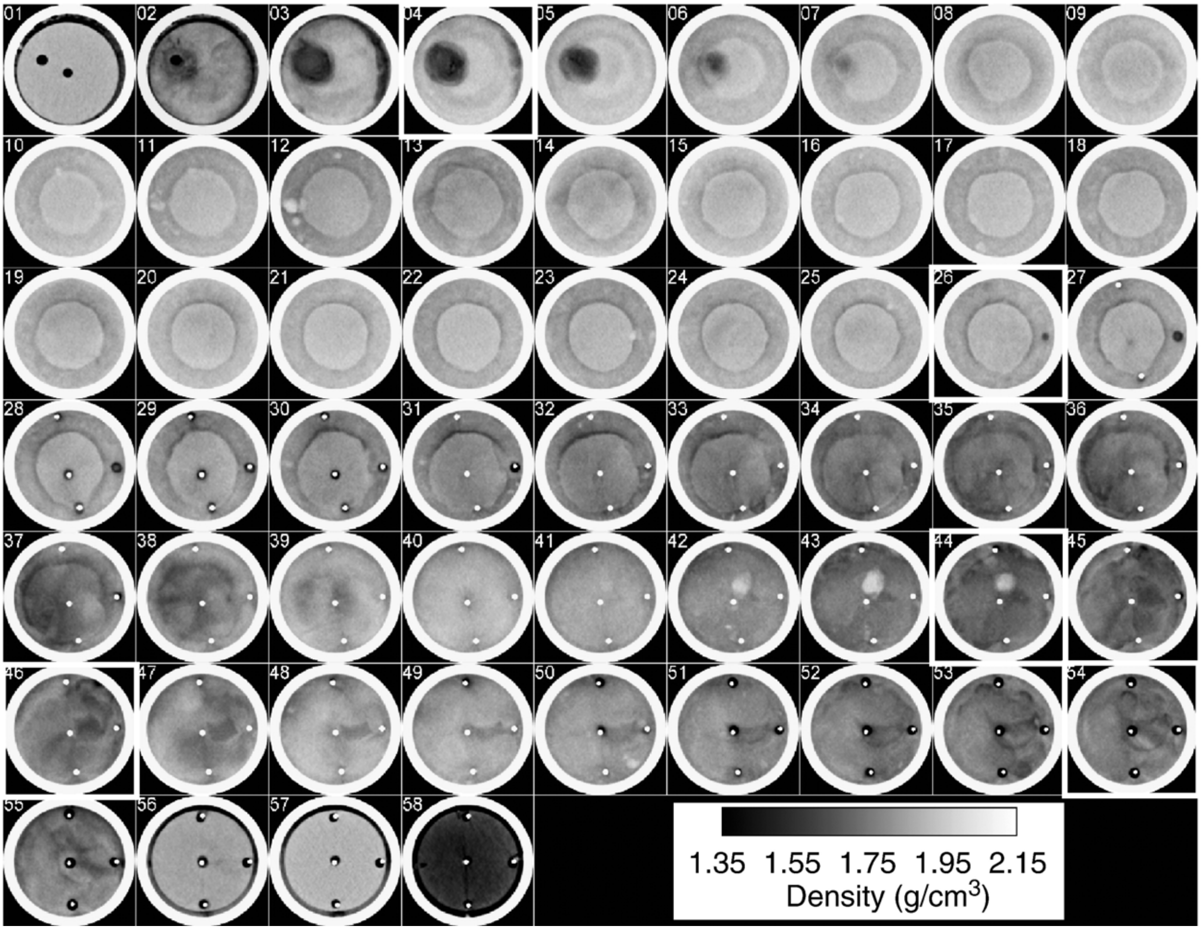

Fig. 5. Fifty-eight sequential 0.5 cm scans of the vessel (white circle) and sample. The first scan is of the Teflon spacer with a center hole and the gas port (off center). The low-density regions located adjacent to the gas port in Cross Sections 2–7 indicate drying that occurred during preliminary testing. The ring visible in Cross Sections 2–29 is the result of the hydrate formation/dissociation from the preliminary test, not a packing artifact. Less dense regions (e.g. Scan 52) around the thermocouples (small white circles in Scans 27–58) are a result of poor packing. Other heterogenieties, such as higher density spots in Cross Sections 12, and 42 through 44 are probably the result of poor sand–water mixing. Cross Sections 4, 26, 44, 46, and 54 are identified by white boxes.

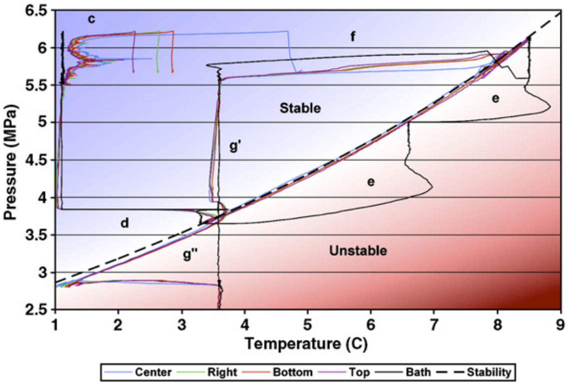

Fig. 6. Hydrate formation (c), stable thermal test (d), dissociation by thermal stimulation (e), second hydrate formation (f), stable depressurization (g′), and dissociation by depressurization and thermal stimulation (g″). The methane hydrate stability curve (dashed) separates the thermodynamically stable and unstable regions.

brighter (e.g., the circular aluminum vessel wall [ρ= 2.7 g/cm^3] depicted as white) and lower density regions are darker (e.g., the region outside of the aluminum vessel containing the water/propylene glycol coolant [ρ=~1 g/cm^3] depicted as black). Five scan locations (Scans 4, 26, 44, 46, and 54, identified in Fig. 5 by white outlines) were selected as having interesting features, and these are discussed throughout this paper. Scan 4 contains a low-density region caused by water loss from passing dry gas through in the preliminary tests. Scan 26 contains a low-density ring, in addition to a poorly packed region near the end of a thermocouple. The low-density ring is presumed to be the result of making and dissociating the hydrate in the preliminary test, and not a packing artifact. Future tests will identify the cause of this ring, but it may be caused by a process similar to frost heaving. Scans 44, 46, and 54 also display heterogeneities, including a high-density spot (Scan 44) and variable density between the center and right thermocouple in Scans 46 and 54. Although not immediately apparent in Fig. 5, a vertical density gradient (likely as a result of a gravitationally induced water saturation gradient) is present, resulting in a density of 1.78 at the sample top and 1.85 at the sample bottom.

3. Tests

The test sequence was as follows:

a. Preliminary tests, including vessel strain monitoring during pressurization, hydrate formation, and dissociation
b. A series of mild thermal perturbations to allow estimation of the sand/water/gas (SWG) thermal properties
c. Hydrate formation in the vessel
d. Thermal perturbation under hydrate-stable conditions to allow estimation of thermal properties of the sand/hydrate/water/gas (SHWG) system
e. Thermal stimulation causing hydrate dissociation
f. Hydrate formation
g. Depressurization coupled with thermal stimulation causing dissociation

Each of these tests are described below except for the preliminary tests, which are discussed only in the context of how they may have affected the subsequent tests. Tests c through g are shown in Fig. 6, along with the methane hydrate stability curve.

3.1. Pre-test

Hydrate formation and dissociation was induced in the vessel to monitor vessel strain as the hydrate formed and dissociated. No CT scanning was performed prior to or during this test. Strain gages were glued to the vessel before it was placed into an incubator set to about 4 °C. We pressurized the vessel multiple times with nitrogen to examine the stress-strain curve prior to pressurization with methane for the first hydrate formation. Hydrate may form with nitrogen, though not at the pressures and temperatures we were applying. The gases used in the strain test were dry, and repeated filling and emptying of the dry gas removed some water from the system, causing a drier region near the gas inlet port, affecting later tests. The water content in the sand following the completion of all the tests was quantified gravimetrically. The final filling was with methane, upon which hydrate was formed and then dissociated by depressurization. During the

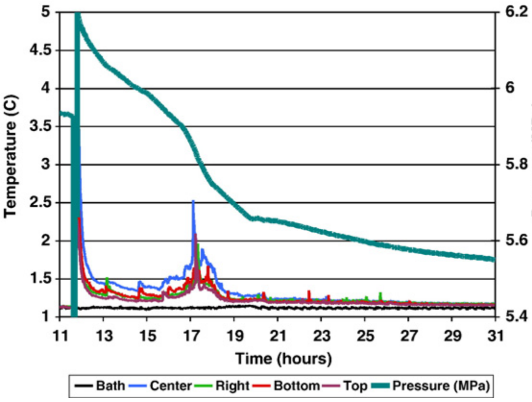

Fig. 7. Temperatures and pressure during hydrate formation.

depressurization, temperatures fell below the ice point (to −2.0 °C). Other than a slight reduction in the quantity of water available for subsequent hydrate formation on account of venting initially dry gas, we expected no irreversible physical changes in the system resulting from these tests. However, upon CT scanning, we observed the features shown in Fig. 5.

3.2. Thermal test

To provide data to calculate thermal properties of the SWG system and to allow comparison to a corresponding SHWG system, we performed a thermal test prior to hydrate formation. Methane hydrate and water possess similar thermal conductivities [0.5 $\mathrm{Wm^{-1}\,K^{-1}}$ (Cook and Leaist, 1983) vs. 0.58 $\mathrm{Wm^{-1}\,K^{-1}}$ (Incropera and DeWitt, 1981) respectively], whereas the thermal conductivity for the quartz which composes the sand is 6.2 to 10.4 $\mathrm{Wm^{-1}\,K^{-1}}$ (Incropera and DeWitt, 1981) and the thermal conductivity for methane is ~0.03 to 0.04 $\mathrm{Wm^{-1}\,K^{-1}}$ for the conditions of interest here (Lemmon et al., 2003). Substantial differences in the overall thermal conductivity of the medium containing water or hydrate would indicate differences in the configuration of the sand, water, hydrate, and gas in the system. These data and the inverse modeling used to estimate thermal conductivity are discussed in Moridis et al. (2005).

3.3. Hydrate formation

The pressure vessel was connected to a 3.81 L steel bottle, and both were pressurized to 6.2 MPa and then

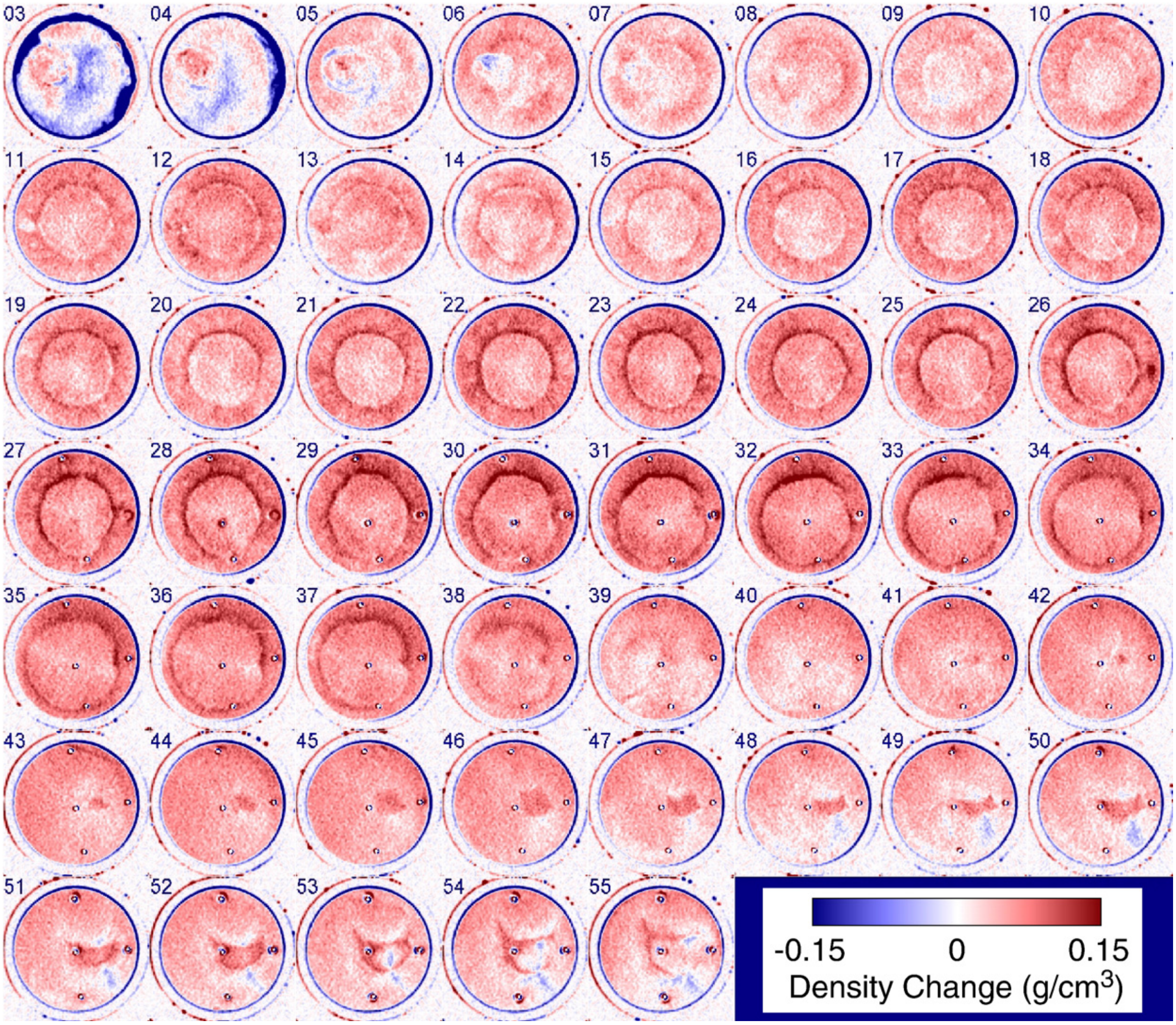

Fig. 8. Density changes ($\mathrm{g/cm^3}$) occurring during pressurization and hydrate formation. Density increases are red, decreases are blue, and no change is white.

Table 1
Processes affecting CT density

Process	Range	Voxel density change (g/cm^3)
Hydrate formation or dissociation (same water mass)	0 to 100% conversion (or dissociation)	0 to ~0.03 (or ~0.03 to 0)
Water saturation changes (changing water mass)	0 to 100% water saturation	0 to ~0.38
Mechanical deformation (changing porosity, same water mass)	2% porosity change	0.03
Gas pressure	0 to 6.1 MPa	~0.05

isolated from the methane supply. The temperature of the vessel containing the moistened sand was maintained at 1.1 °C, whereas the bottle was at room temperature. Two indicators of hydrate formation are observed in the data (Fig. 7). Because of the exothermic nature of hydrate formation, upon pressurization, temperatures in the vessel exceed the bath temperature (by as much as 3.8 °C), indicating hydrate formation (and methane compression). The second indication is the decline in pressure occurring because the formation of hydrate consumes methane from the gas phase. Both of these occur simultaneously during the formation. Hydrate formation does not proceed at a constant rate, but occurs in fits and starts, as can be seen from the jagged temperature curves in Fig. 7; here, a significant amount of formation occurs over about 1 d. Temperatures increase the most in the center of the vessel, because heat transfer occurs primarily through conduction to the temperature-controlled bath. Since the path length to the center is the longest, the center has the poorest heat transfer to the bath. In this hydrate formation, 1.49 mol of methane were converted into hydrate, indicating at least 65% of the water was converted to hydrate based on a hydration number of 5.75. Most of the remaining water remained in the liquid state because the temperature was above the freezing point, although some excess water was possibly present in the hydrate phase because of suboptimal hydrate cage occupancy.

Density differences determined by CT between the starting (unpressurized) condition and hydrate formation are shown in Fig. 8. In these images, increased density (red) is observed almost throughout the sample, with the largest increases occurring where the density was initially lowest on account of poor packing (e.g., Fig. 8, Cross Section 26). In a few regions towards the sample ends (e.g., Fig. 8, Cross Sections 6 and 50), isolated regions of decreased density (blue) occur in the initially denser regions. These difference images also appear to show a low-density rind appearing between the vessel wall and the sample. This rind will be discussed further below.

In our tests, density differences observed by CT can be caused by four primary processes: hydrate formation, water saturation changes, mechanical changes (compaction), and gas pressure changes. We refer to density here as the mass per voxel volume in g/cm^3. Any increase in mass in a voxel will result in an increase in density. Therefore, in a voxel containing gas, water, and sand, the formation of hydrate requires the addition of gas molecules. The mass increase results in a density increase, despite the fact that the density of pure methane hydrate (about 0.917) is less than the density of the water initially present. The magnitudes of expected density changes resulting from the four processes are shown in Table 1. Observed changes may in fact be the result of all four processes. From Table 1, water saturation changes can clearly swamp the other processes.

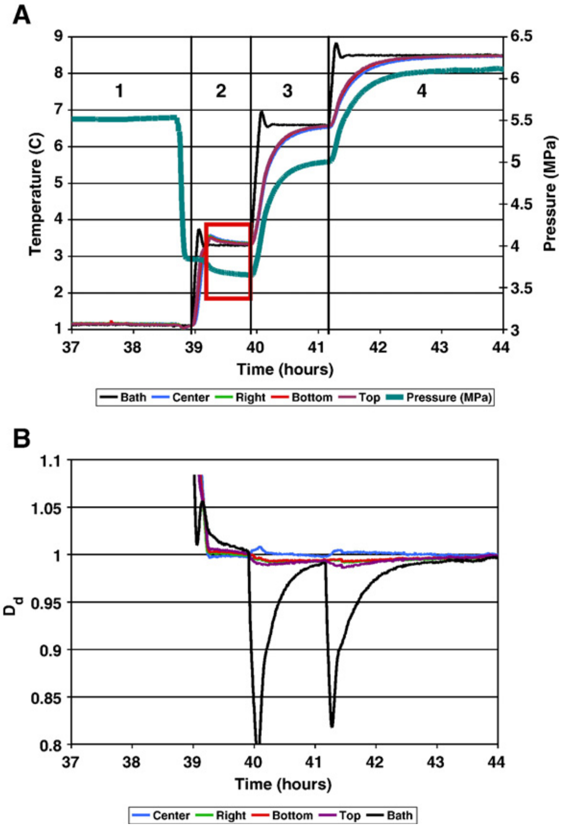

Fig. 9. (A) Temperature and pressure during thermal dissociation; (1) lowering the pressure to approach equilibrium point, (2) thermal test with hydrate present [note hydrate formation – red box], (3) and (4) dissociation by thermal stimulation. (B) Degree of disequilibrium over the same time period.

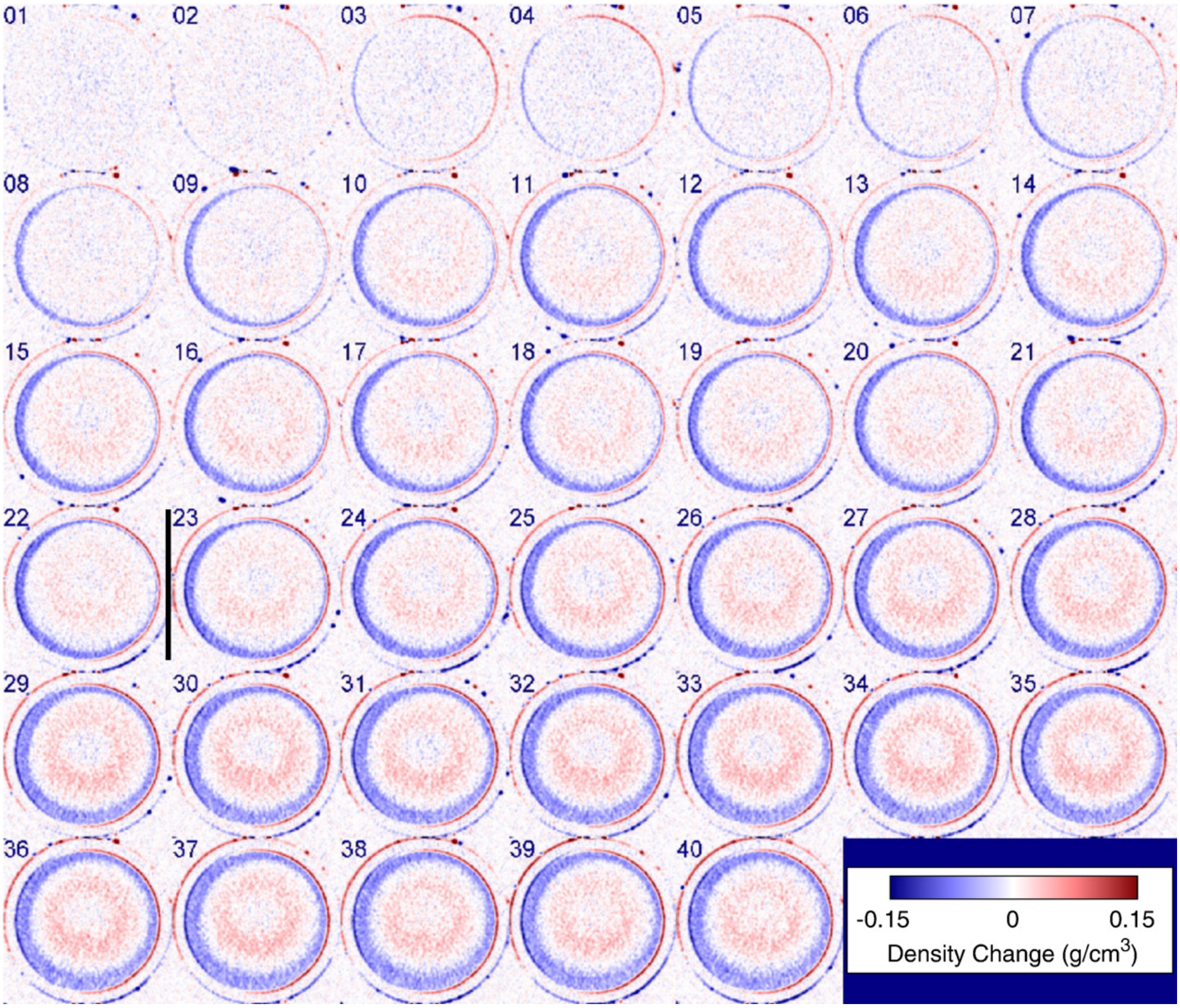

Fig. 10. Difference tomograms for thermal stimulation. Density reductions are due to dissociation and water saturation changes; density increases are primarily caused by water saturation changes. The black line between Scans 22 and 23 indicates the time when the temperature was increased.

3.4. Thermal dissociation

About 27 h after beginning hydrate formation, the volume of the headspace was changed to increase the sensitivity of the pressure response. Thus, Bottle 3 (3809 mL) was closed to the vessel, and Bottle 1 (159.5 mL – previously containing air at ambient conditions) was opened. The pressure in the system was vented to reduce the pressure to 3.82 MPa, inducing a slight temperature decline as a result of gas expansion, and the temperature was allowed to stabilize (Fig. 9A). To gather data on the thermal properties of the SHWG system, the bath temperature was increased to 3.38 °C. At this pressure and temperature, methane hydrate is stable. The change in conditions induced more hydrate formation (simultaneous pressure decline with increased temperature) in spite of the declining hydrate formation driving force. At 39.9 h, the temperature was increased to 6.58 °C to induce dissociation, and at 41.2 h, the temperature was raised to 8.48 °C to induce further dissociation.

Fig. 9B presents the degree of disequilibrium (D_d) for the thermal dissociation. The D_d is a relative measure of the how close the system is to equilibrium and is defined in Eq. (1):

$$D_\mathrm{d} = \frac{P_\mathrm{meas}}{P_\mathrm{eq}(T_\mathrm{meas})} \quad (1)$$

where P_meas is the measured pressure, and P_eq is the calculated equilibrium pressure at the measured temperature (T_meas) at the thermocouple locations. Values equal to or greater than 1 indicate conditions in which methane hydrate is stable, and values less than 1 indicate unstable conditions. The equilibrium pressures were calculated from an algorithm presented by Moridis (Moridis et al., 2004). Initially, the D_d was much greater than one, but through depressurization, temperature increase, and hydrate formation, equilibrium was reached just prior to 39.9 h. The D_d for the bath was plotted also as a measure of the driving force.

When the temperature was increased to 6.58 °C, instability occurred at the three outermost thermocouple locations. This is indicated by the slight decrease in the D_d at these locations, but increased stability occurred at the center. The increase in stability is caused by the increase in pressure attributable to the dissociating hydrate near the vessel wall, prior to warming at the center. Instability occurred in the center approximately 0.5 h later. When the bath temperature was increased to 8.48 °C, unstable conditions occurred again at the outer thermocouple locations and increased stability occurred at the center. After about an hour, the center became slightly unstable, and then trended back towards the equilibrium curve ($D_d = 1$). Note that on the second thermal step, the top was the first to become unstable in spite of the presence of the rind, while the bottom and right sides continued towards recovery from the first thermal step. After a small sudden decrease in the degree of disequilibrium at all four thermocouple locations at 41.45 h, all conditions tended to return towards equilibrium.

Density differences for the thermal dissociation are presented in Fig. 10. In this figure, two nearby locations (24 and 25 in Fig. 5, near the sample center but away from the thermocouples) were scanned sequentially over most of the duration of thermal dissociation, and the initial densities from the two cross sections were subtracted from the corresponding subsequent densities. The two central nearby locations were selected to provide good temporal resolution of changes, and two nearby cross sections with similar packing away from possible end effects yielded a coherent record of the dissociation. Images 1 through 22 were collected sequentially over the duration of the first temperature increase, and the remaining images were collected during the second temperature increase. Changes caused by dissociation begin to become apparent in Image 3, with a slight reduction in density on the left near the vessel wall, and become larger and larger over time. Note that density increases in some locations, even though only decreases were expected because dissociation and mass removal from a voxel reduces the density. These increases occurred in the central region (but not the center) and were likely a result of water saturation changes (water migration) in response to the dissociation front and hydrate formation, as discussed below, and possible compaction from increased capillarity (Ghezzehei and Or, 2000).

Examination of the images in Fig. 10 reveals that the density changes were not symmetrical. Dissociation occurred from the outside-in as expected, but occurred preferentially away from the upper right quadrant. This is probably because the thermal conductivity in the low-density rind is lower than other locations, reducing heat transfer in this region.

From the data shown in Fig. 10, we constructed an axial temporal cross section. This vertical cross section is plotted as the background in Fig. 11. It is useful to compare these changes with the changes in methane content in the sample and average density over time. In the first temperature increase, 0.37 mol of methane was produced; in the second temperature increase, 0.33 mol of methane was produced. These methane quantities were calculated using measured pressure, temperature, and volume, and the equation of state from Lemmon et al. (2003). Volume changes from hydrate formation and dissociation were accounted for the calculations. As expected, the dissociated hydrate curve approximately mirrors the somewhat noisy average density change curve, but does not mirror it exactly, owing to gas pressure increase in the vessel.

Figs. 10 and 11 clearly show that the dissociation occurs from the outside-in, and the movement of the front is clear. The approximate location of the dissociation front is identified in Fig. 11 at the bottom and top by a thin black line, and is clearly asymmetrical, because the locations of the front on the top and bottom are

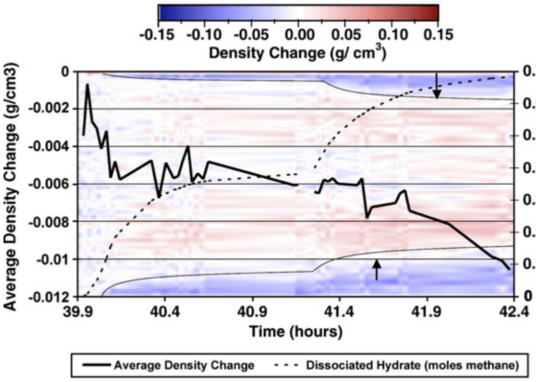

Fig. 11. Changes in average density (heavy line), moles of methane produced from hydrate (dotted line), and spatial distribution of density changes over a vertical cross section (background). The apparent location of the dissociation front is indicated by the thin line and an arrow.

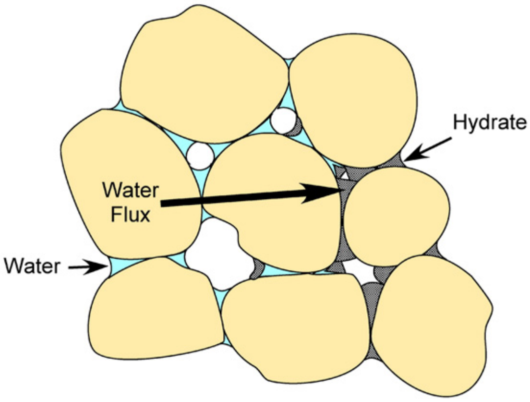

Fig. 12. Conceptual model of a capillary pressure gradient induced by the presence of hydrate in a porous medium. The hydrate is assumed to be water wetting and causes the pores available to water and gas to be smaller, effectively increasing the capillary pressure difference from the water (only) – containing porous medium.

different. The decrease in density behind the front is significantly greater than is possible by dissociation alone, and the concomitant density increase inside the front indicates that water saturation changes have occurred, and that water has moved towards the sample center.

To explain the density changes, we present a conceptual model of a partially water-saturated water-wetting porous medium in which a gradient in hydrate saturation exists locally on account of hydrate formation (or dissociation) from one direction (Fig. 12). Hydrate formation consumes a portion of the water present in the porespace, partially to fully filling the available porespace with solid hydrate (right side of Fig. 12). We assume that the hydrate is water-wetting (either pore filling or cementing), which is justified by its outer surface being composed of water molecules. The porous medium containing the hydrate will act like a porous medium having smaller pores, because hydrate now partially fills the pores. Just as water will flow from a wide capillary tube into a narrow one, water flows towards the location containing hydrate as a result of the enhanced capillarity there. Thus, a moving formation or dissociation front will drag a water saturation front along.

3.5. Second hydrate formation

Following the thermal dissociation tests and allowing 14.6 h after the bath had reached 8.64 °C for equilibration, the bath temperature was reduced to 3.75 °C (a temperature at which methane hydrate is stable at the pressure maintained), and Bottle 3 was reconnected to provide a gas reservoir to supply methane for hydrate formation (Fig. 13). This hydrate formation occurred temporally much more uniformly than the first, and in less than 2 h, whereas the initial formation took over 20 h. The thermal dissociaton steps discussed above did not result in complete dissociation. Thus, hydrate was present in some locations, and nucleation was unnecessary – a situation different from the memory effect in which hydrate from partially organized water structure remaining from previously contained hydrate (Schroeter et al., 1983; Sloan et al., 1998; Uchida et al., 2000).

Fig. 14 shows the changes in average density over the second hydrate formation, along with the number of moles of methane converted. The background shows the density changes in a central vertical cross section. As with the dissociation, the formation front moved inward from the vessel wall. The magnitude of the density change indicates that the change results from water migration as a result of the changing capillary pressure

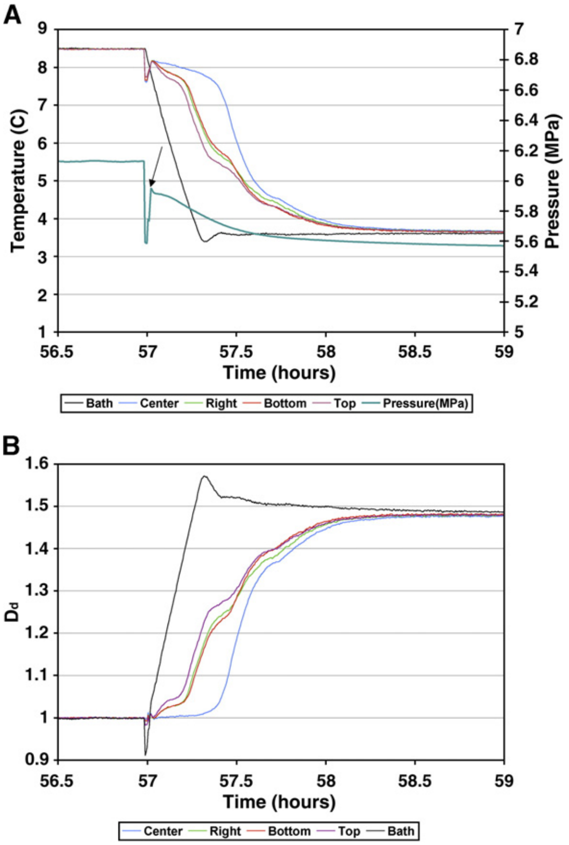

Fig. 13. (A) Pressure and temperatures recorded during the second hydrate formation; Arrow indicates time when Bottle 3 was connected; (B) Degree of disequilibrium over that duration.

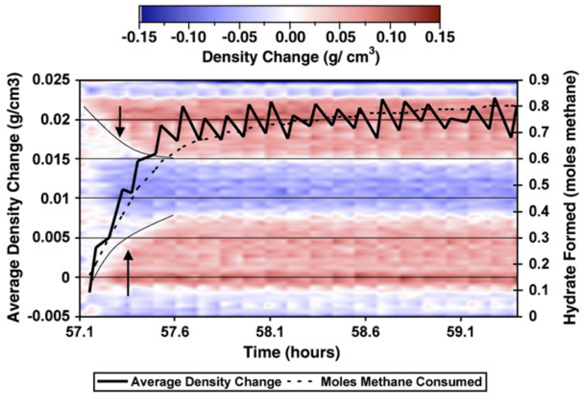

Fig. 14. Average change in density (heavy line) and moles of methane converted to hydrate (dashed line) during the second hydrate formation. These plots overlie a temporal vertical cross section showing density changes within the vessel. The formation front is indicated by the thin black line and the arrows.

gradient upon hydrate formation. As the front moved inward, little hydrate formed near the vessel wall, because the water had earlier migrated towards the mid-radius region in the thermal dissociation steps. New hydrate formation in the mid-radius region then drew water from the center region, causing the center density to decrease significantly.

3.6. Dissociation by depressurization and thermal stimulation

After hydrate formation finished, the pressure in the vessel was lowered to near the equilibrium pressure (Fig. 15). Cooling occurred because of gas expansion, but the pressure decrease triggered additional hydrate formation (pressure decline with excess temperature), so that the temperature exceeded the controlled temperature. At 62.25 h, the pressure was rapidly vented through a back-pressure regulator set at about 2.89 MPa, and the gas was collected and quantified in a Marriotte bottle.

On depressurization, the temperature in the sample initially approached the hydrate stability point (0.97 °C) prior to increasing. Temperatures at the three outer thermocouples increased towards the bath temperature over several hours. This is much slower than the temperature increase prior to hydrate formation, which occurred over tens of minutes. The temperature at the center, presumed to be the lowest temperature in the system because of its distance to the controlled bath temperature, leveled out at about 1.3 °C for over an hour ($P_{eq}=2.95$ MPa). This nonequilibrium behavior indicates that heat transfer, mass transfer, or kinetics limited the dissociation.

After more than an hour at 1.3 °C, the temperature in the sample center rapidly increased towards the bath temperature. As expected, the gas collection curve simultaneously leveled out as the center temperature approached the bath temperature, indicating the completion of hydrate dissociation. Fig. 16 shows the average density change, moles of methane collected (from both depressurization and dissociation), and the location of the dissociation front over time. There was an initial overall decrease in density very early (first few minutes after 62.3 h) due to the depressurization. This decrease was followed by a dissociation front moving inward from the vessel wall, caused by thermal stimulation, which began shortly afterwards (where the slope of the gas collection curve changes). As expected, the average density change mirrors the evolution of methane from the system. An increase in density is observed in the center of the sample, which we attribute

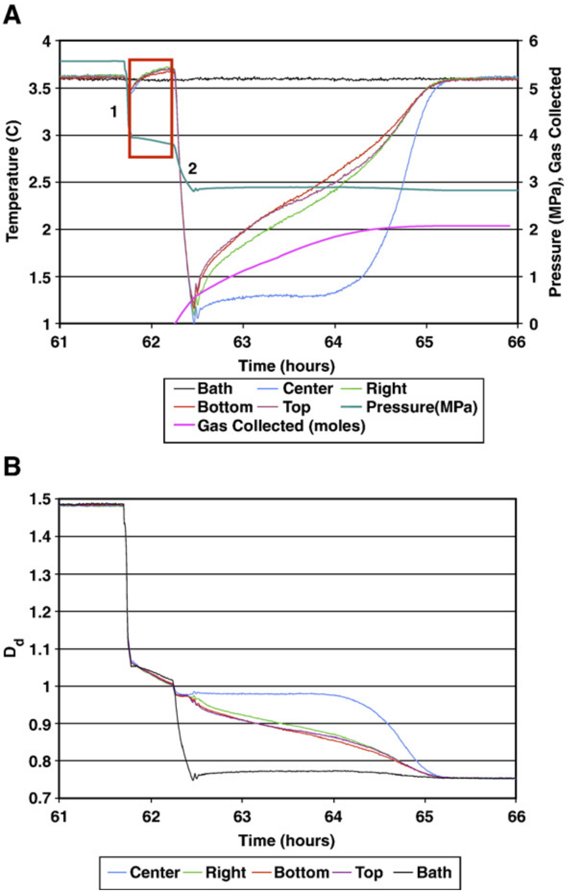

Fig. 15. (A) Pressure and temperatures during depressurization. Reduction in pressure to approach equilibrium (1), and depressurization induced dissociation (2). Note hydrate formation on pressure reduction (red box); (B) Degree of disequilibrium over that duration.

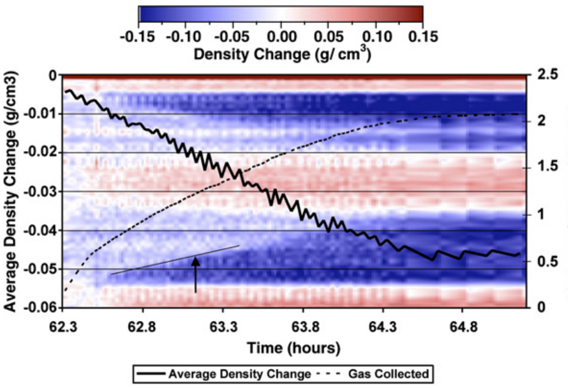

Fig. 16. Average density change (heavy line), moles of gas collected (dashed line), and location-specific density along the vertical cross section over the depressurization and thermal stimulation. The apparent location of the dissociation front is indicated by the thin black line and the arrow.

primarily to water released from the hydrate moving back to drier regions by capillarity.

4. Discussion

This paper describes a set of tests in which methane hydrate was formed multiple times and dissociated using different techniques. Pressure, temperature, and density (through CT) measurements were made to attempt to quantify these processes and observe the system behaviors. None of these techniques individually or in pairs is sufficient to adequately characterize the system investigated. Without the CT scanning, we would have initially attributed what we observed in both formation and dissociation tests to bulk phenomena. With the scanning data, however, we have a means of examining spatially occurring behavior and validating numerical models.

During the course of the experiments, several unexpected phenomena occurred. One was the change in water saturation that followed the hydrate (formation or dissociation) front. In these tests, water saturation changes affected the density much more strongly than hydrate formation, dissociation, gas pressure changes, or mechanical processes. The changing water saturation affects other properties as well, such as thermal conductivity, and water and gas relative permeability.

Another unexpected occurrence was that the rate of hydrate formation could be dramatically increased by reducing the driving force (reducing the pressure towards the equilibrium pressure at the prevailing temperature, or increasing the temperature towards the equilibrium temperature at the prevailing pressure – see boxed regions in Figs. 11 and 15). We offer two possible explanations. First, as hydrate forms, some of the water may lose contact with the gas phase because the hydrate forms between the water and gas phases, creating isolated pockets of water containing dissolved methane. When gas pressure declines or temperature increases, these pockets become overpressured, and outgassing methane breaks hydrate walls, improving communication between the gas and water phase. The other explanation is that the equilibrium saturation of methane in water decreases with decreasing pressure or increasing temperature. As pressure drops or temperature increases in the system, the water suddenly becomes supersaturated with respect to methane, providing methane for hydrate formation. Either a reduction in pressure or increase in temperature may cause an exsolution of methane in this water, causing the opening of a pathway for the gas to flow and increasing the formation rate.

4.1. Mass balance

The quantity of methane hydrate formed and dissociated was calculated from measured pressure and temperature data, known volumes, and accepted methane properties (Lemmon et al., 2003). The initial hydrate formation consumed 1.49 moles of methane. The final water content, based on gravimetric analysis of 25 samples, was 237 g (13.16 mol). This indicates that the initial conversion was 65%, based on a hydration number of 5.75. In the first thermal dissociation step, 0.37 moles of methane was produced from dissociation; in the second, 0.33 mol was produced. The second hydrate formation added 0.81 mol of methane to hydrate, resulting in a total of 1.60 mol in hydrate. The small miscellaneous hydrate formations resulted in an additional 0.04 mol of methane being confined in hydrate. The final depressurization/thermal stimulation produced 2.07 mol of methane – 1.63 from hydrate and the remainder from gas present in the pore space. The overall mass balance, including the final system venting, was within 10% of the expected value. Errors stem from the lack of temperature measurement in the Marriotte bottle, errors in volume measurements, and possible leaks.

4.2. Nonequilibrium behavior

Kinetics or mass transfer may have limited the final dissociation (depressurization/thermal stimulation) step. In this step, a constant temperature (~1.3 °C) and pressure (2.89 MPa) were established for over an hour in the center of the sample. This condition is not identical to the equilibrium condition (for 1.3 °C, 2.95 MPa, or 1.1 °C, 2.89 MPa).

A possible explanation for the nonequilibrium behavior is measurement error. The thermocouples were calibrated before and after the experiment against a precision mercury thermometer that had been externally calibrated. The reported error of the standard at 0.01 °C is less than 0.1 °C. Error in the internal temperature measurement and calibration at 0.1 °C adds an additional ~0.04 °C, resulting in a maximum expected temperature error of 0.14 °C. Temperatures presented in this paper were adjusted to match the equilibrium temperatures for a set of equilibrium conditions (following the second thermal stimulation step). Correction magnitudes were 0.12 to 0.16 °C. This is justified because the equilibrium conditions are well known, and thus can be used as a calibration standard, with the adjustments generally within the estimated temperature error. The pressure transducer was calibrated before the test against a Druck DPI 610 pressure calibrator. The error in pressure measurement at 2 to 5 MPa total pressure was approximately 0.007 MPa. No additional corrections were made in the pressure data presented. The thermocouples and pressure transducer behaved as expected for all other parts of the test, and thus we do not believe that measurement error explains the nonequilibrium behavior.

To rule out mass transfer limitations, we need to know the permeability and relative permeabilities in the SHWG system. These were not measured directly, but are considered below. Because the pressure was measured outside the sample, the pressures at the thermocouple locations within the sample were higher than the indicated pressure to force gas flow through the medium. If we assume that the hydrate dissociates uniformly and the methane gas properties are constant throughout the sample despite the pressure difference, the pressure through the sample would be

$$P = \frac{q\mu x}{k}\left(L - \frac{x}{2}\right) + P_{\mathrm{meas}} \tag{2}$$

where P (Pa) is pressure, q ($\mathrm{m^3/m^3 s}$) is the volumetric gas generation rate (methane generated per volume of sample), x (m) is the location from 0 to the length of the vessel (L), k ($\mathrm{m^2}$) is the permeability, μ (Pa s) is the viscosity, and P_{meas} (Pa) is the measured pressure. We are interested in the pressure difference ($P - P_{\mathrm{meas}}$) from the measured pressure to the midpoint of the vessel (the location of the thermocouple):

$$P - P_{\mathrm{meas}} = \frac{3q\mu L^2}{8k} \tag{3}$$

Our gas generation rate was about $1.5 \times 10^{-4}\ \mathrm{m^3/m^3\ s}$ at 1.3 °C and 2.89 MPa, L is 0.267 m, and viscosity is 10.934 μPa s. This requires the permeability to be $7.3 \times 10^{-16}\ \mathrm{m^2}$ to induce the pressure difference adequate to keep the pressure in the vessel center at an equilibrium pressure of 2.95 MPa.

The Kozeny–Carmen equation (Freeze and Cherry, 1979) is a simple technique to roughly estimate permeability for sands with known grain size distributions.

$$k = \left(\frac{n^3}{(1-n)^2}\right)\frac{d_{\mathrm{m}}^2}{180} \tag{4}$$

Here, n is the porosity (0.38), and d_{m} is the representative grain size, taken here as the grain diameter at which 10% of the particles by mass are finer, and 90% coarser (~75 μm) (Das, 1985). This gives a dry, no-hydrate-present permeability of $4.4 \times 10^{-12}\ \mathrm{m^2}$, which is about 6000 times greater than the permeability needed to cause the pressure difference needed to induce the measured nonequilibrium temperature. Though we expect the presence of water and hydrate will restrict the permeability of the sand, we do not have a good sense of the relative permeability behavior of SHWG systems. Further measurements are needed to identify the cause of the nonequilibrium behavior.

In our analysis, we assumed that the methane properties (density, viscosity) were constant over the pressures encountered in the vessel. If we conservatively use 1% of the Kozeny–Carmen permeability to calculate pressures for evaluation of methane properties, the pressure varies by .001 MPa across the vessel. At the system pressure, this minor change in pressure will not cause large differences in methane properties; thus, our assumption that they remain constant is reasonable. We also assumed that the gas generation was uniform throughout the volume. From the CT scans, we know that dissociation occurs from the outside to center, but occurs fairly uniformly along the sample length. Therefore, the gas flow to the outlet would still encounter the entire sample (although the outer rind would be encountered more preferentially because of the decreased water saturation and the increased void space caused by the change in volume from dissociation). This approximation may not be valid, considering the uneven saturation distribution that developed as a result of hydrate formation and dissociation.

4.3. Rind

CT images showed an apparent low-density rind between the sample and the vessel wall that was produced upon the formation of hydrate (Fig. 17). No rind was initially observed despite the pre-test hydrate

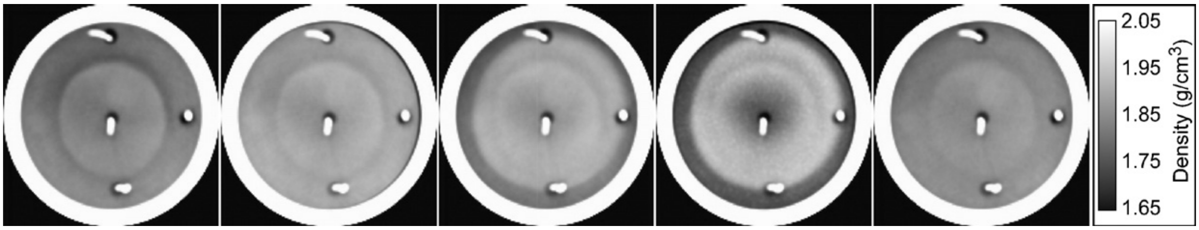

Fig. 17. Average density of 51 (of the 58) cross sections. (a) Initial condition, no rind. (b) After hydrate formation, [note rind on upper right side between vessel (white) and the sample], (c) after thermal stimulation (no rind), (d) after second hydrate formation (note rind on top), and (e) after depressurization, no rind.

formation. In the scan performed following the initial hydrate formation, a rind less than 1 mm thick formed over as much as a 180° arc on the top right side. On dissociating the hydrate by thermal stimulation, the rind appeared to diminish. On reforming hydrate, a larger rind up to 1 mm wide formed over an arc of about 230° over the top of the sample. Upon dissociation, the rind again appeared to diminish.

The density along a transect (inset Fig. 18) that crosses the interface between the sample and the pressure vessel wall at two locations (including the location of the rind [top] and location where there is no apparent rind [bottom]) is shown in Fig. 18 for five conditions: (1) before hydrate formation, (2) after hydrate formation, (3) after thermal dissociation, (4) after second hydrate formation, and (5) after dissociation by depressurization and thermal stimulation. The transect begins and ends in aluminum, and because of that, it is longer than the inner diameter of the vessel. The before-hydrate-formation curve begins in the aluminum (high density), continues through a small low-density region near the vessel wall (which occurs in all the profiles), trends downward over a centimeter or so to the bottom edge of the "ring" (caused by preliminary test changes), and declines and increases over the next 4 cm to the top edge of the ring where density again declines. At this point, the density increases to some extent, crosses a small low-density region similar to the one on the other side of the vessel, and ends in the high-density aluminum. The general trend also shows the density gradient caused by the gravitationally induced water saturation gradient resulting in densities from about 1.85 near the bottom to about 1.81 g/cm^3 near the top. The after-hydrate-formation curve shows higher density across the sample and is somewhat similar in shape except at the top, where the rind was produced and the density declines about 0.1 g/cm^3. Thermal dissociation redistributes the water such that

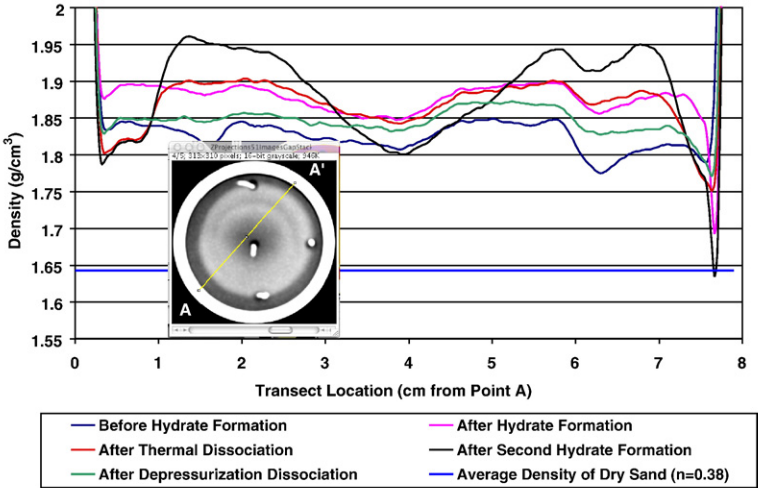

Fig. 18. Rind properties. Density across Transect A-A′ (inset) before hydrate formation, following hydrate formation, following thermal dissociation, following the second hydrate formation, and after dissociation by depressurization and thermal stimulation. The average density of dry sand is shown for comparison.

there is a wide (0.5 cm) low-density ring at the outside of the sample, the center is higher density, and the density in the rind recovers about 0.05 g/cm^3, but not completely.

The second hydrate formation caused the density to decrease slightly at the lower vessel/sample interface. The density in the mid-radius region increased significantly, but the density in the center declined to its lowest values because hydrate formation was occurring from the outside in, and the water was being drawn from the center to the mid radius region. During this second hydrate formation, a dominant rind appeared at the top, with voxel densities near that of dry sand at the same porosity. On dissociation from depressurization and thermal stimulation, the densities across the transect returned to nearly the original values but slightly higher, because of the pressure difference between measurements, with a slight rind remaining at the top.

The indicated densities in Fig. 18 clearly show that the rind has a minimum density greater than 1.6 g/cm^3. The resolution of the CT images is such that we cannot distinguish a void smaller than $0.25 \times 0.25 \times 5$ mm. Therefore, a narrow (<0.25 mm) gap would be interpreted as a low density region. The density observed is greater than the density of the gas, water, or hydrate phases, but about equal to the density of the dry silica sand at the original packing density. The resolution of the CT images is not sufficient to determine the exact composition of the rind (gas, hydrate, water, and sand).

A possible explanation for the rind is that hydrate forms from the vessel wall inwards as observed by Huang and Fan (2005), because this is where the driving force is greatest due to low heat transfer resistance. Hydrate formation “dries” the medium, inducing water flow towards the wall. This new water also forms hydrate near the wall in the sand. The process continues, forming a less dense region due to dilution of the sand by hydrate, with hydrate formation moving farther in with the temperature front. The outer locations might become “solid” with hydrate and sand, compacting the sand in the center. In the mid radius region, the sand becomes slightly compacted and when hydrate forms there, water is imbibed from the center. Thus, the density increases in the mid-radius region, while decreasing in the center. Upon dissociation, the sand/water system expands to fill the rind. This occurs because the dissociation front travels from the vessel wall inwards. Because the thermal conductivity of the silica sand is an order of magnitude larger than either water or hydrate, heat will flow inwards through sand grains. Hydrate near the sand/hydrate interface will dissociate most easily at the contact because of the heat transfer and the presence of a diffuse double layer in the water, concentrating ions and inhibiting hydrate presence. The gas from dissociation forms small bubbles between the hydrate and the sand grains towards the outside, pushing the grains back towards the vessel. Because the process proceeds from the outside towards the inside, the sand grains are pushed back and held there by capillary adhesion.

Another possible explanation for the rind is that hydrate formation could begin away from the vessel wall, and the front moves inward. The water near the vessel wall is then drawn by capillarity towards the hydrate formation front, drying the rind. Upon dissociation, the water is released from the hydrate and flows towards the vessel walls by capillarity and vapor transport. This explanation seems unlikely without a reason for the hydrate to begin forming away from the vessel wall.

4.4. Stepwise changes

Fig. 19 shows the density of the five cross sections identified in Fig. 5 initially, as a result of hydrate formation, thermal stimulation, second hydrate formation, and dissociation by depressurization and thermal stimulation. Also shown is the net change over the experiment. In Fig. 19B, we see that the density generally increases throughout the sample. This is expected because of hydrate formation, and because of the pressure change between this data set and the initial data set. As mentioned above, the increase in density is greater for the originally less dense (more poorly packed) regions. In the first cross section, decreased density is observed to the right and below the drier spot, which has increased density. It is likely that water flowed, causing this density change. Although not clear here, a rind also formed.

Following thermal stimulation of this SHWG system (Fig. 19C) significant density decreases were observed in the approximately centimeter thick ring near the vessel wall where dissociation occurred. Density increases are observed in the mid-radius ring inward from the dissociated zone. The second hydrate formation (Fig. 19D) caused density to increase further in the mid-radius ring, owing to hydrate formation and water movement, a decrease in the center region as a result of water movement, and a slight decrease in the outer ring resulting from strong hydrate formation or water movement. A rind also formed during this step but is not visible due to slight alignment differences.

Fig. 19E shows density changes that occurred during dissociation from depressurization and thermal

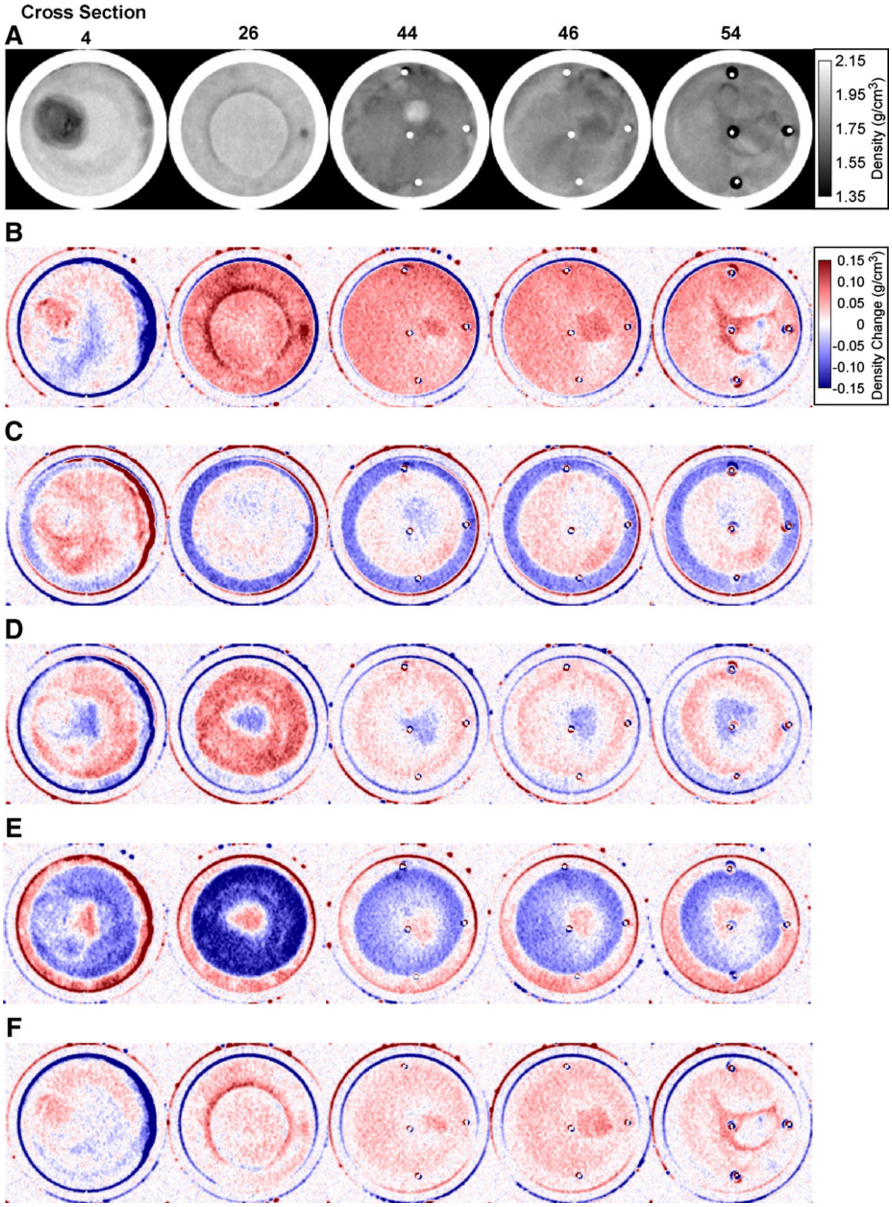

Fig. 19. (A) Initial density and step-wise density changes (B) difference between initial and following hydrate formation, (C) difference between b. and following thermal stimulation, (D) difference between c. and following second hydrate formation, (E) difference between d. and following depressurization and thermal stimulation, and (F) overall density change from initial.

stimulation. Density decreased significantly in the mid radius region, and increased in the center and outer ring, consistent with water previously held by capillarity and hydrate moving from the higher to the lower density regions. Fig. 19F shows the overall density change from the original density. An overall density increase was expected and observed, because of the difference in gas pressure between the two conditions. Additionally, larger density increases can be seen in the more poorly packed regions, because of the gas pressure difference impacting those areas to a larger extent. Compaction of the sand from the beginning to end of the tests was not observed. Visual comparison of the size of the poorly packed region around the thermocouples (Scan 54) shows no difference between the initial set of scans and the final set, indicating no significant compaction occurred resulting from the hydrate formation and dissociation steps.

5. Conclusions

Many processes occurred during the experiments performed on hydrate formation and dissociation in partially saturated sand. These include vapor-phase mass transfer of methane and water, liquid-phase mass transfer of water, heat transfer, and hydrate formation and dissociation. Numerical simulation of hydrate formation and dissociation that may occur in reservoirs upon the production of methane gas from hydrate reserves needs to consider these processes.

Our use of CT to observe these experiments illustrated some very important occurrences as a result of hydrate formation and dissociation, including water migration and the formation of a rind. Heat transfer and relative permeability are affected by the saturations of the phases present; as such, these properties are affected by water movement. Evaluation of the importance of this on a larger scale by both experimentation and simulation is needed, to evaluate this effect on the production of natural gas from a hydrate-bearing reservoir.

The reason the rind formed between the sample and the vessel wall upon hydrate formation is not well understood. The mechanism behind the rind requires elucidation to determine whether it is a mechanical effect or a hydrological effect. For the purposes of extraction of natural gas from a reservoir, this occurrence may or may not be important, but for understanding laboratory data that provide a partial basis of our understanding of gas hydrates and allows us to validate our models, this requires further investigation.

The rate of hydrate formation is not always proportional to the driving force in a porous medium. We have seen rate increases when the driving force decreases for both pressure reduction and temperature increase. This may not be significant for natural gas production from a hydrate bearing reservoir, but poses an interesting question: is the hydrate formation rate not intrinsically a function of the driving force, or are other physics causing this to happen?

Using multiple means of measurement is critical for understanding hydrate behavior. Here, CT was used in addition to pressure and temperature measurements. The future incorporation of additional measurement techniques is important in helping to interpret existing data for a greater understanding of hydrate behavior.

Acknowledgments

The authors wish to acknowledge John A. Apps, Dan Hawkes, and Bill Waite for their helpful comments in reviewing this manuscript. This work was supported by the Assistant Secretary for Fossil Energy, Office of Natural Gas and Petroleum Technology, through the National Energy Technology Laboratory, under the U.S. DOE, Contract No. DE-AC03-76SF00098.

References

Clarke, M., Bishnoi, P.R., 2001. Determination of the activation energy and intrinsic rate constant of methane gas hydrate decomposition. Can. J. Chem. Eng. 79 (1), 143–147.

Cook, J.G., Leaist, D.G., 1983. An exploratory study of the thermal conductivity of methane hydrates. Geophys. Res. Lett. 10 (5), 397–399.

Das, B.M., 1985. Principles of Geotechnical Engineering. PWS Publishers, Boston. 571 pp.

Freeze, R.A., Cherry, J.A., 1979. Groundwater. Prentice-Hall, Inc. 604 pp.

Ghezzehei, T.A., Or, D., 2000. Dynamics of soil aggregate coalescence governed by capillary and rheological processes. Water Resour. Res. 36 (2), 367–379.

Handa, Y.P., Stupin, D., 1992. Thermodynamic properties and dissociation characteristics of methane and propane hydrates in 70A radius silica gel pores. J. Phys. Chem. 96, 8599.

Huang, D., Fan, S., 2005. Measuring and modeling thermal conductivity of gas hydrate-bearing sand. J. Geophys. Res. 110 (B01311). doi:10.1029/2004JB003314.

Incropera, F.P., DeWitt, D.P., 1981. Fundamentals of Heat Transfer. John Wiley and Sons, New York. 819 pp.

Kim, H.C., Bishnoi, P.R., Heidemann, R.A., Rizvi, S.S.H., 1987. Kinetics of methane hydrate decomposition. Chem. Eng. Sci. 42 (7), 1645–1653.

Lemmon, E.W., McLinden, M.O., Friend, D.G., 2003. Thermophysical properties of fluid systems. In: Linstrom, P.J., Mallard, W.G. (Eds.), NIST Chemistry WebBook, NIST Standard Reference Database. National Institute of Standards and Technology, Gaithersburg MD. http://webbook.nist.gov.

Moridis, G.J., Collet, T.S., Dallimore, S.R., Satoh, T., Hancock, S., Weatherill, B., 2004. Numerical studies of gas production from several CH4 hydrate zones at the Mallik site, Mackenzie Delta, Canada. J. Pet. Sci. Eng. 43, 219–238.

Moridis, G.J., Seol, Y., Kneafsey, T.J., 2005. Studies of reaction kinetics of methane hydrate dissociation in porous media. Fifth International Conference on Gas Hydrates (ICGH 5)Trondheim, Norway. LBNL-57298.

National Resource Council, 2004. Charting the Future of Methane Hydrate Research in the United States. 192 pp.

Schroeter, J.P., Kobayashi, R., Hildebrand, M.A., 1983. Hydrate decomposition conditions in the system H_2S–methane–propane. Ind. Eng. Chem. Fundam. 22, 361–364.

Sloan, E.D., 1998. Clathrate Hydrates of Natural Gases, second ed. Marcel-Dekker, Inc, New York. 705 pp.

Sloan, E.D., Subramanian, S., Matthews, P.N., Lederhos, J.P., Khokhar, A.A., 1998. Quantifying hydrate formation and kinetic inhibition. Ind. Eng. Chem. Res. 37, 3124–3132.

Stern, L.A., Kirby, S.H., Durham, W.B., 1996. Peculiarities of methane clathrate hydrate formation and solid-state deformation, including possible superheating of water ice. Science 273 (5283), 1843–1848.

Stern, L.A., Kirby, S.H., Circone, S., Durham, W.B., 2004. Scanning electron microscopy investigations of laboratory-grown gas clathrate hydrates formed from melting ice, and comparison to natural hydrates. Am. Mineral. 89 (8–9), 1162–1175.

Uchida, T., Ebinuma, T., Narita, H., 2000. Observations of CO_2-hydrate decomposition and reformation processes. J. Cryst. Growth 217, 189–200.

Waite, W.F., Winters, W.J., Mason, D.H., 2004. Methane hydrate formation in partially water-saturated Ottawa sand. Am. Mineral. 89, 1202–1207.

Winters, W.J., Pecher, I.A., Waite, W.F., Mason, D.H., 2004. Physical properties and rock physics models of sediment containing natural and laboratory-formed methane gas hydrate. Am. Mineral. 89 (8–9), 1221–1227.